Pushing the boundaries of chemistry? It takes #HumanChemistry

Make your curiosity and talent as a chemist matter to the world with a specialty chemicals leader. Together, we combine cutting-edge science with engineering expertise to create solutions that answer real-world problems. Find out how our approach to technology creates more opportunities for growth, and see what chemistry can do for you at:

evonik.com/career

EVONIK
Leading Beyond Chemistry

ADVANCED MATERIALS
www.advmat.de

Overcoming Intensity Saturation in Nonlinear Multiple-Quantum-Well Metasurfaces for High-Efficiency Frequency Upconversion

Nikita Nefedkin, Ahmed Mekawy, Jonas Krakofsky, Yongrui Wang, Alexey Belyanin, Mikhail Belkin, and Andrea Alù**

Engineered intersubband transitions in semiconductor heterostructures featuring multiple quantum wells (MQWs) are shown to support record-high second-order nonlinear susceptibilities. By integrating these materials in metasurfaces with tailored optical resonances, it is possible to further enhance photonic interactions, yielding giant nonlinear responses in ultrathin devices. These metasurfaces form a promising platform for efficient nonlinear processes, including frequency upconversion of low-intensity thermal infrared radiation and harmonic generation, free of phase-matching constraints intrinsic to bulk nonlinear crystals. However, nonlinear saturation at moderately large pump intensities due to the transfer of electron population into excited subbands facilitated by strongly enhanced light–matter interactions in metasurfaces fundamentally limits their overall efficiency for various nonlinear processes. Here, the saturation limits of nonlinear MQW-based metasurfaces for mid-infrared frequency upconversion are significantly extended by optimizing their designs for excitation with a strong pump coherently coupled with unpopulated upper electron subbands. This counterintuitive pumping scheme, combined with tailored material and photonic engineering of the metasurface, avoids saturation at practical levels of continuous-wave pump intensities, yielding significantly larger upconversion efficiencies than in conventional approaches. The present results open new opportunities for nonlinear metasurfaces, less limited by saturation mechanisms, with important implications for night-vision imaging and compact nonlinear wave mixing systems.

1. Introduction

Flat optical components[1] are gaining significant attention in the photonics and nanoelectronics communities because of their ability to greatly compactify and integrate traditional optical components such as lenses, and their ability to precisely control the wavefront of light. The technology is based on metasurfaces consisting of arrays of subwavelength nanoinclusions, which make it possible to control the local amplitude and phase of reflected or transmitted optical beams with unprecedented resolution.[2,3] Flat optical components may also be designed to implement nonlinear optical phenomena over an ultrathin platform.[4–7] Their constituent elements support large field confinement[8] and may be engineered to provide efficient phase control[4,9,10] and frequency mixing[11,12] of light waves.

A particular class of ultrathin nonlinear metasurfaces consists of tailored metallic nanoresonators loaded with multiple-quantum-well (MQW) semiconductor heterostructures, which have been shown to provide a giant nonlinear response due to engineered intersubband transitions.[13] These metasurfaces combine optimal field enhancements with the large second-order susceptibility of MQWs,[11,12,14,15] yielding a record nonlinear response, orders of magnitude larger than the one of traditional nonlinear materials.[16] In addition, they offer the unique feature of eliminating phase matching constraints for mixing processes, since the nonlinear processes arise locally within each nanoresonator composing the surface. Despite these advantages, the overall frequency conversion

N. Nefedkin, A. Mekawy, A. Alù
Photonics Initiative
Advanced Science Research Center
City University of New York
New York, NY 10031, USA
E-mail: nnefedkin@gc.cuny.edu; aalu@gc.cuny.edu

A. Mekawy
Department of Electrical Engineering
City College of The City University of New York
New York, NY 10031, USA

The ORCID identification number(s) for the author(s) of this article can be found under https://doi.org/10.1002/adma.202106902.

DOI: 10.1002/adma.202106902

J. Krakofsky, M. Belkin
Walter Schottky Institute
Technical University of Munich
85748 Garching, Germany

Y. Wang, A. Belyanin
Department of Physics and Astronomy
Texas A&M University
College Station, TX 77843, USA

A. Alù
Physics Program
Graduate Center
City University of New York
New York, NY 10016, USA

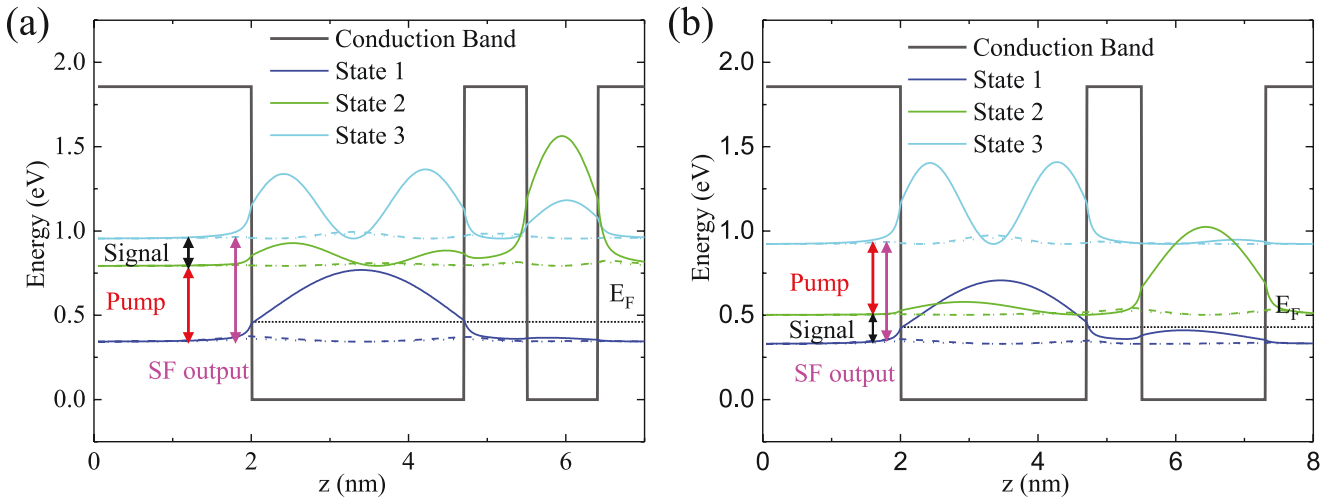

Figure 1. Multi-quantum-well semiconductor heterostructures for SFG: a) a strong pump is resonant with the transition between the lower two electron subbands; b) a strong pump is resonant with the transition between the upper two electron subbands. Computed Fermi energy for both structures is shown as a dotted line.

efficiency of of MQW-based metasurfaces is quite limited due to intensity saturation. Consider, for instance, the upconversion scheme based on resonant three-wave mixing within a three-level material utilizing three lowest subbands in an asymmetric coupled quantum well (ACQW) system, in which only the lowest subband is populated with electrons by doping. For resonant pumping of the lowest intersubband transition, electrons will be promoted to the excited subbands, reducing the population differences between the ground and excited sates. The electron population redistribution reduces the second-order nonlinear optical susceptibility, limiting the nonlinear response as well as the total conversion efficiency. Due to the large and typically nonuniform field enhancement in nanoresonators, nonlinear MQW metasurfaces are particularly limited by these saturation phenomena, which kick in at very low pump intensities, implying that their overall nonlinear mixing efficiency peaks at modest inputs.[15]

Here, we explore the optimal design and operation of MQW metasurfaces that greatly alleviate this fundamental limitation, largely enhancing the achievable upconversion efficiency in the infrared frequency range (long wavelength infrared and mid-wavelength infrared radiation to short wavelength infrared, ≈2 μm). We develop MQW structures based on InGaAs/AlAsSb heterostructures grown on InP substrates as a specific prototype; however, the same methodology can be developed for any MQW material system. We perform comparative analysis of MQW designs and pumping schemes to show that the highest-efficiency design includes, counterintuitively, a scheme with a strong pump driving highly excited unpopulated subbands of the MQW structure. We show that the proposed approach largely avoids the detrimental effects of saturation and significantly improves the overall upconversion efficiency of mid-infrared radiation achievable with MQW metasurfaces pumped at practical levels of continuous-wave pump intensities up to ≈1 MW cm^{-2}.

To evaluate the effects of band nonparabolicity and the Coulomb interactions beyond doping-induced space charge,[17] we also developed a model including many-body interactions of carriers in the screened Hartree–Fock approximation. A numerical analysis of this model demonstrates that, at moderate doping levels relevant to the proposed designs, the Coulomb interaction leads mainly to a population-dependent energy shift of the subbands, whereas the magnitude of the nonlinear susceptibility is not affected significantly. The energy shifts can be compensated by tuning of the pump laser frequency.

Our optimal material and metasurface design, tailored in combination with the pumping scheme, is shown to largely mitigate the saturation of the second-order response and achieves a conversion efficiency of about 4% in the 8 to 2 μm upconversion process.

2. Optimized Heterostructures and Pumping Schemes

2.1. MQW Designs for Alternative Pumping Schemes

In this section, we consider two different heterostructures optimized for different pumping schemes. The conduction band structures and computed electron states that we consider are shown in **Figure 1**, tailored to maximize the upconversion efficiency in the case of two alternative schemes of resonant pumping: pumping the lower transition and pumping the upper transition within the three-level system formed by the lowest three subbands of the MQW system. These two different pumping schemes result in different MQW designs for optimal excitation and efficient upconversion.

The MQWs were designed with a self-consistent Schrödinger–Poisson solver using an 8-band kP model and including thermal population of the electron subbands.[18] From the electron wavefunctions provided by the solver, the transition dipole moments as well as the nonradiative scattering rates, based on electron–phonon scattering, were calculated. All material parameters were taken from ref. [19]. To provide high nonlinear susceptibility for an 8 to 2 μm upconversion, the wells and barriers have been optimized to produce a doubly-resonant nonlinear response for the target pumping scheme, and to

maximize the product of three transition dipole moments in the expression for the second-order nonlinear susceptibility for the resonant sum-frequency generation (SFG) processes.[16] The presented ACQW designs also consider the limitations of practical structure growth by molecular beam epitaxy and are based on materials that are lattice-matched to InP.

The optimized layer sequence of the coupled $In_{0.53}Ga_{0.47}As/AlAs_{0.56}Sb_{0.44}$ quantum wells (in nanometers) is **1.0**/2.7/**0.8**/1.8/**1.0** for the MQW designed for pumping the lower transition and **1.0**/2.7/**0.8**/0.9/**1.0** for the one designed to pump the upper transition where the $AlAs_{0.56}Sb_{0.44}$ barriers are shown in bold. The MQWs are designed to use uniform silicon n-doping in the $In_{0.53}Ga_{0.47}As$ wells (normal font). In the case of the structure designed for strong resonant pumping of the transition between the upper two electron subbands, the doping level is set equal to 6.25×10^{18} cm^{-3} which results in a Fermi energy being 70 meV smaller than the lower transition energy. For the MQW designed for strong resonant pumping of the optical transition between the first two electron subbands, the doping level is set to 8.0×10^{18} cm^{-3} which results in the same sheet doping density for the two structures. Effects of the Coulomb interactions beyond the overall space charge are included in the theory developed later in Section 5.

Figure 1 shows the band structures of the optimized MQWs. The parameters of these optimized structures are listed in **Table 1**.

In Figure 1 and further in the text, we denote the states taking part in the SFG process from the lowest energy to the highest energy as $|i\rangle$, $i = 1, 2, 3$. We denote the incident and output fields in the schemes as E_1, E_2, and E_3. E_2 is the output field at the SF in both structures shown in Figure 1. For the conventional pumping scheme, Figure 1a, E_1 is a strong field pumping the $1 \rightarrow 2$ transition, whereas E_3 is a weak signal field interacting primarily with the $2 \rightarrow 3$ transition. In the alternative scheme in which we pump the upper transition $2 \rightarrow 3$, on the contrary, the pumping field E_3 is much stronger than the signal field E_1.

Table 1. Computed intersubband transitions parameters for the heterostructures designed for upper and lower states pumping.

Lower transition pumping	Upper transition pumping
Transition frequencies in meV	
$\omega_{21} = 453$	$\omega_{21} = 156$
$\omega_{32} = 162$	$\omega_{32} = 459$
$\omega_{31} = 615$	$\omega_{31} = 615$
Transition dipole moments in nm	
$z_1 = 0.69$	$z_1 = 1.18$
$z_2 = 0.46$	$z_2 = 0.51$
$z_3 = 1.21$	$z_3 = 0.66$
Decay rates of states populations in ps^{-1}	
$r_{21} = 0.12$	$r_{21} = 0.5$
$r_{32} = 0.65$	$r_{32} = 0.07$
$r_{31} = 0.2$	$r_{31} = 0.23$
Linewidths in meV	
$\gamma_{21} = 15$	$\gamma_{21} = 7.5$
$\gamma_{32} = 7.5$	$\gamma_{32} = 15$
$\gamma_{31} = 22.5$	$\gamma_{31} = 22.5$
Doping densities in cm^{-3}	
$N = 8 \times 10^{18}$	$N = 6.25 \times 10^{18}$

2.2. Nonlinear Response for Sum-Frequency Generation

To introduce the relevant quantities that describe the upconversion process, we assume normally incident monochromatic fields $\mathbf{E}_1(\omega_1)$ and $\mathbf{E}_3(\omega_3)$,[12] written as

$$\mathbf{E}^{\text{inc}}(\mathbf{r},t) = \vec{\mathcal{E}}_1(\mathbf{r})e^{-i\omega_1 t} + \vec{\mathcal{E}}_3(\mathbf{r})e^{-i\omega_3 t} + \text{c.c.} \tag{1}$$

where $\vec{\mathcal{E}}_i(\mathbf{r})$ is the slowly varying amplitude of the ith EM field. The bichromatic field (1) induces in the nonlinear medium a polarization current which oscillates with frequency $\omega_2 = \omega_1 + \omega_3$. We can express the nonlinear polarization as[16]

$$\mathcal{P}_j^{(2)} = 2\varepsilon_0 \sum_{k,l} \chi_{jkl}^{(2)}(\omega_1 + \omega_3; \omega_1, \omega_3)\, \mathcal{E}_{1,k}\mathcal{E}_{3,l}, \tag{2}$$

where ε_0 is the free-space permittivity, j, k, l are polarization indices, x or y.

Our goal is to consider arbitrarily strong pumping fields beyond the second-order perturbation approximation. We can still parameterize the nonlinear response with the tensor $\chi_{jkl}^{(2)}$ in Equation (2), but for strong enough pumping, the tensor becomes intensity-dependent.

For the materials considered in this work, $\chi_{zzz}^{(2)}(I_{1,z}, I_{3,z}; \mathbf{r})$ is the only nonzero intrinsic second-order susceptibility tensor element of the metasurface unit cell, and it depends on the local intensities of the z-polarized fields, $I_{1,z}$ and $I_{3,z}$, with frequencies ω_1 and ω_3 inside the MQW structure.

The intensities are expressed through the fields as[16,20]

$$I_{i,z} = 2\varepsilon_0 n(\omega_i) c\, |\, \mathcal{E}_{i,z}\, |^2 \tag{3}$$

They are related to the incident pump intensities I_i^{inc} as

$$I_{i,z} = I_i^{\text{inc}} n_{\text{MQW}}(\omega_i) \left| \frac{\mathcal{E}_{i,z}}{\mathcal{E}_i^{\text{inc}}} \right|^2 \tag{4}$$

where $n_{\text{MQW}}(\omega_i)$ is the refractive index of MQW at ω_i, and the term $\left|\mathcal{E}_{i,z}/\mathcal{E}_i^{\text{inc}}\right|$ is the local field enhancement.

Below, we calculate the nonlinear susceptibility of the structure under consideration, $\chi_{zzz}^{(2)}$, for both pumping schemes introduced in Section 2.1. It will be then used to calculate the upconversion efficiency η_{SFG}, which we define as the ratio of the SF field intensity, I_2 in our notation, and the intensity of the weak signal field, I_w, which can be either I_1 or I_3 depending on the pumping scheme (see Figure 1):

$$\eta_{\text{SFG}} = \frac{I_2}{I_w^{\text{inc}}},\ w = 1 \text{ or } 3 \tag{5}$$

2.3. Model for MQWs Interacting with EM Fields

In this section, we model the subbands in the MQW structure as a 3-level system (3LS) with fixed transition frequencies and

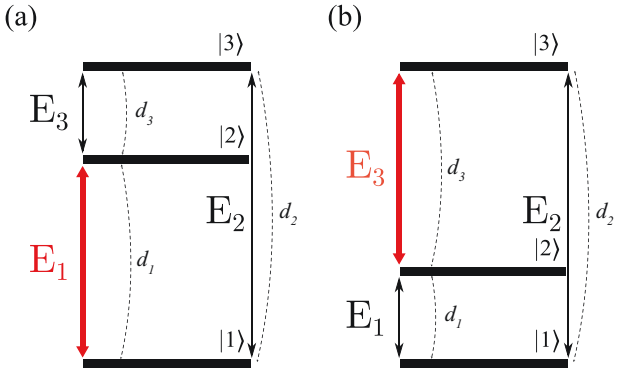

Figure 2. 3LS schemes modeling the subbands in a realistic MQW structure: a) conventional scheme, pumping the lower transition (E_1 scheme); b) the proposed scheme, pumping the upper transition (E_3 scheme). The thick red arrows denote the strong pumping field.

dipole matrix elements, calculated as described in the previous section.[15,21,22] Here, we are interested in an SFG process and therefore consider the three lowest subbands involved in the SFG (see Figure 1) neglecting transitions to higher subbands. The transition frequencies between these lowest subbands we denote as $\omega_{ij}, i \neq j$, where $i, j = 1, 2, 3$ and indicate the subband number. The dipole moments between the subbands we denote as d_1 for the lowest transition, $1 \rightarrow 2$, d_2 for the transition $1 \rightarrow 3$, and d_3 for the upper transition, $2 \rightarrow 3$.

The two types of MQW structures and the corresponding relevant EM fields are shown in **Figure 2**. They correspond to the two pumping schemes introduced in Section 2.1, namely, the more conventional scheme where the pumping is applied to the lower transition (panel a) and the proposed scheme of upper transition pumping (b). In Figure 2, we see two incident fields, E_1 and E_3, one of which is a strong pumping field, E_s, denoted as a thick red arrow, and the other is a weak signal field, E_w. The SF output field is E_2. For brevity, in what follows, we will refer to the pumping scheme of the lower transition as the E_1 scheme, and the pumping scheme of the upper transition as the E_3 scheme.

The model presented in this section is a simplified description of a many-body dynamics of carriers in the phase space, where all scattering processes are included in **k**-independent phenomenological relaxation rates. The dipole moments, energy levels, relaxation rates, and wave functions are calculated based on the band structure described in Section 2.1 using the self-consistent Poisson–Schrödinger solver and the Fröhlich Hamiltonian for electron-phonon coupling.[23] Despite its relative simplicity, this model grasps the main features of light–matter interaction and allows us to model analytically the SFG efficiency taking into account saturation, power broadening, and off-resonant interactions beyond the rotating wave approximation (RWA).

To describe the system shown in Figure 2, we introduce the Hamiltonian $H = H_{\text{RWA}} + H_{\text{non-RWA}}$

$$\begin{aligned} H_{\text{RWA}} = {} & \hbar\omega_{21}|2\rangle\langle 2| + \hbar\omega_{31}|3\rangle\langle 3| + \\ & \hbar\left(e_1 e^{-i\omega_1 t} + e_1^* e^{i\omega_1 t}\right)\left(|1\rangle\langle 2| + |2\rangle\langle 1|\right) + \\ & \hbar\left(e_2 e^{-i\omega_2 t} + e_2^* e^{i\omega_2 t}\right)\left(|1\rangle\langle 3| + |3\rangle\langle 1|\right) + \\ & \hbar\left(e_3 e^{-i\omega_3 t} + e_3^* e^{i\omega_3 t}\right)\left(|2\rangle\langle 3| + |3\rangle\langle 2|\right) \end{aligned} \tag{6}$$

$$\begin{aligned} H_{\text{non-RWA}} = {} & \hbar\left(e_{3,2} e^{-i\omega_3 t} + e_{3,2}^* e^{i\omega_3 t}\right)\left(|1\rangle\langle 3| + |3\rangle\langle 1|\right) + \\ & \hbar\left(e_{3,1} e^{-i\omega_3 t} + e_{3,1}^* e^{i\omega_3 t}\right)\left(|1\rangle\langle 2| + |2\rangle\langle 1|\right) + \\ & \hbar\left(e_{1,2} e^{-i\omega_1 t} + e_{1,2}^* e^{i\omega_1 t}\right)\left(|1\rangle\langle 3| + |3\rangle\langle 1|\right) + \\ & \hbar\left(e_{1,3} e^{-i\omega_1 t} + e_{1,3}^* e^{i\omega_1 t}\right)\left(|2\rangle\langle 3| + |3\rangle\langle 2|\right) \end{aligned} \tag{7}$$

where $e_{i,j} = \mathcal{E}_i d_j/\hbar$ is the Rabi frequency of the ith EM field coupled to the jth intersubband transition in the MQW structure; d_j is the dipole moment of the jth transition, $j = 1, 2, 3$, where $1 \equiv 2 \rightarrow 1$, $2 \equiv 3 \rightarrow 1$, and $3 \equiv 3 \rightarrow 2$ (see Figure 2). If the indices coincide, $i = j$, we use a shorthand, $e_i \equiv e_{i,i}$. The Hamiltonian consists of two parts, namely the RWA part, Equation (6), which describes the resonant interactions of the EM field with the MQW transitions, and the off-resonant (non-RWA) part, Equation (7), which includes the interactions of the strong pump field with the other two dipole transitions that have resonant frequencies that are far from the frequency of the strong pump field. Depending on which pumping scheme we study, the non-RWA Hamiltonian contains the first two terms for the E_3 scheme or the last two terms for the E_1 scheme.

Starting from the Hamiltonian $H_{\text{RWA}} + H_{\text{non-RWA}}$, we can derive the equations of evolution for the density matrix ρ, also known as optical Bloch equations.[24,25] We provide the details of the derivation in the Supporting Information.

The nonlinear polarization $\mathcal{P}_z^{(2)}(\omega_2) = \varepsilon_0 \chi_{zzz}^{(2)} \mathcal{E}_{1,z} \mathcal{E}_{3,z}$ is determined by the off-diagonal density matrix elements. The nonlinear polarization associated with the SFG process is mainly due to the component of ρ_{ij} oscillating with sum frequency, that is, close to the frequency of the $3 \rightarrow 1$ transition. By using the ansatz, $\rho_{31} \rightarrow \sigma_{31}\exp(-i\omega_2 t)$, we move to the expression for the slow varying polarization $\mathcal{P}_z^{(2)}(\omega_2)$ in terms of σ_{31}: $\mathcal{P}_z^{(2)}(\omega_2) = N d_2 \sigma_{31}^{(2)}$, where N is the doping density.[24,26] In Supporting Information, we find the expression for $\sigma_{31}^{(2)}$ valid for any pumping strength and associate it to $\chi_{zzz}^{(2)}$ through the relation

$$\chi_{zzz,s}^{(2)} = \frac{N}{2\varepsilon_0} \frac{\sigma_{31,s}^{(2)}}{\mathcal{E}_1 \mathcal{E}_3} d_2 \tag{8}$$

where s denotes the strong pumping field, either E_1 or E_3 depending on the chosen pumping scheme.

3. Comparison of the two Pumping Schemes

In this section, we consider specifically the upconversion process from 8 to 2 µm, and calculate the susceptibility functions for both studied pumping schemes.

3.1. Second-Order Nonlinear Optical Susceptibilities for E_1 and E_3 Pumping Schemes

Using the density matrix equations and the relationship between the off-diagonal element σ_{31} with the second-order nonlinear optical susceptibility function $\chi_{zzz,s}^{(2)}$, Equation (8), we can calculate the susceptibility function for the SFG process. For the 3LS introduced in the previous section, we can get full analytic formulas for $\chi_{zzz,s}^{(2)}$ in the steady state, but they are very cumbersome (see Supporting Information for details). Therefore, we

present the result as a color map versus the values of the signal and pump frequencies (cf. Figure 1) in **Figure 3**.We see that the maximum values of $|\chi^{(2)}_{zzz}|$ for both structures arise when the signal and pump frequencies are near the frequencies of the $1 \rightarrow 2$ and $2 \rightarrow 3$ intersubband transitions. The resonances of the second-order susceptibility function for the E_3 pumping scheme are narrower than for the E_1 scheme, and the peak values are ≈2.5 times higher. In addition, the $|\chi^{(2)}_{zzz,E_1}|$ function in the scheme when the pump is applied to the lower transition has a dip associated with effective absorption and, consequently, with the saturation of $1 \rightarrow 2$ transition. The negative effect of this saturation on the $\chi^{(2)}_{zzz,E_1}$ function will be discussed below.

To derive simplified expressions for the $\chi^{(2)}_{zzz,s}$ functions, we assume exact resonances, that is, $\omega_{21} = \omega_1$, $\omega_{31} = \omega_2$, $\omega_{32} = \omega_3$, and neglect the inhomogeneous broadening related to band nonparabolicity. After cumbersome algebra shown in the Supporting Information, we come to the following expressions obtained from the stationary solution of the optical Bloch equations. The function $\chi^{(2)}_{zzz,E_1}$ for the conventional E_1 pumping scheme is

$$\chi^{(2)}_{zzz,E_1} = \frac{N}{2\varepsilon_0} \times d_1 d_2 d_3 \times \left[\frac{|e_1|^2 (r_{31}+r_{32})(\omega_1-\omega_3)^2}{2\left(\gamma_{31}\gamma_{32}+|e_1|^2\right)} \times \frac{1}{4|e_1|^2\left(3\gamma_{32}|e_{1,3}|^2+(r_{31}+r_{32})(\omega_1-\omega_3)^2\right)+\gamma_{21}r_{21}(r_{31}+r_{32})(\omega_1-\omega_3)^2} - \frac{r_{21}\gamma_{32}}{4\left(\gamma_{31}\gamma_{32}+|e_1|^2\right)\left(4|e_1|^2+\gamma_{21}r_{21}\right)} \right] \tag{9}$$

The function $\chi^{(2)}_{zzz,E_3}$ for the proposed E_3 scheme is

$$\chi^{(2)}_{zzz,E_3} = -\frac{N}{2\varepsilon_0} \times d_1 d_2 d_3 \times \frac{r_{21}(r_{31}+r_{32})\omega_1^2(\omega_1-\omega_3)^2}{2\left(\gamma_{21}\gamma_{31}+|e_3|^2\right)} \times \frac{1}{8\gamma_{21}|e_{3,1}|^2(r_{31}+r_{32})\omega_1^2+(\omega_1-\omega_3)^2\left(4\gamma_{31}|e_{3,2}|^2(2r_{21}+r_{32})+2r_{21}(r_{31}+r_{32})\omega_1^2\right)} \tag{10}$$

The γ_{ij} are the linewidths (or dephasing rates) of the corresponding transitions, $i \rightarrow j$, and r_{ij} are the population decay rates from i state to j state. We note that electron dephasing rates for intersubband transitions are at least one order of magnitude larger than the population decay rates (i.e., $\gamma_{ij} \gg r_{ij}$). In these formulas for $\chi^{(2)}_{zzz,s}$, along with the power broadening due to the Rabi splitting proportional to $|e_s|^2$, we can see the broadening caused by the coupling of the strong E_s field to the nonresonant transitions, the terms proportional to $|e_{s,1(3)}|^2$ and $|e_{s,2}|^2$. We note that both expressions in Equations (9) and (10) yield real values of $\chi^{(2)}$ in the considered case of resonant excitations.

Using the parameters shown in Table 1 and Equations (9) and (10), we calculate the second-order nonlinear optical susceptibility functions for both pumping schemes. **Figure 4** demonstrates their behavior as a function of the local pumping intensity. We fix the intensity of the weak signal field to be equal to $I_w = 10^{-4}\,\mathrm{W\,cm^{-2}}$, of the same order as the thermal emission from a black body source at 300 K within ≈0.1 μm bandwidth around 8 μm wavelength.

It is seen that the function $\chi^{(2)}_{zzz,E_1}$ changes sign at the critical pumping intensity. This behavior occurs due to the saturation of the lower transition in the MQW structure, namely, $1 \rightarrow 2$. This means that as the pump intensity increases, the population of the first excited subband, ρ_{22}, grows and for a certain value of the pump field, $\mathcal{E}_{0,E_1}$, the second-order susceptibility vanishes. The saturation field, $\mathcal{E}_{0,E_1}$, can be found from Equation (9) as

$$\mathcal{E}_{0,E_1} = \sqrt{\frac{\hbar^2\gamma_{32}r_{21}}{2d_1^2}} \tag{11}$$

Using Equation (3), we obtain the local saturation intensity $I_{0,E_1} \approx 1\,\mathrm{MW\,cm^{-2}}$ for the parameters from Table 1 (cf. Figure 4). At this value of the local intensity in the semiconductor heterostructure, the SFG upconversion scheme with the strong E_1 pump field experiences reduction in the upconversion efficiency. We note that the pumping intensity of 1 MW cm^{-2} is

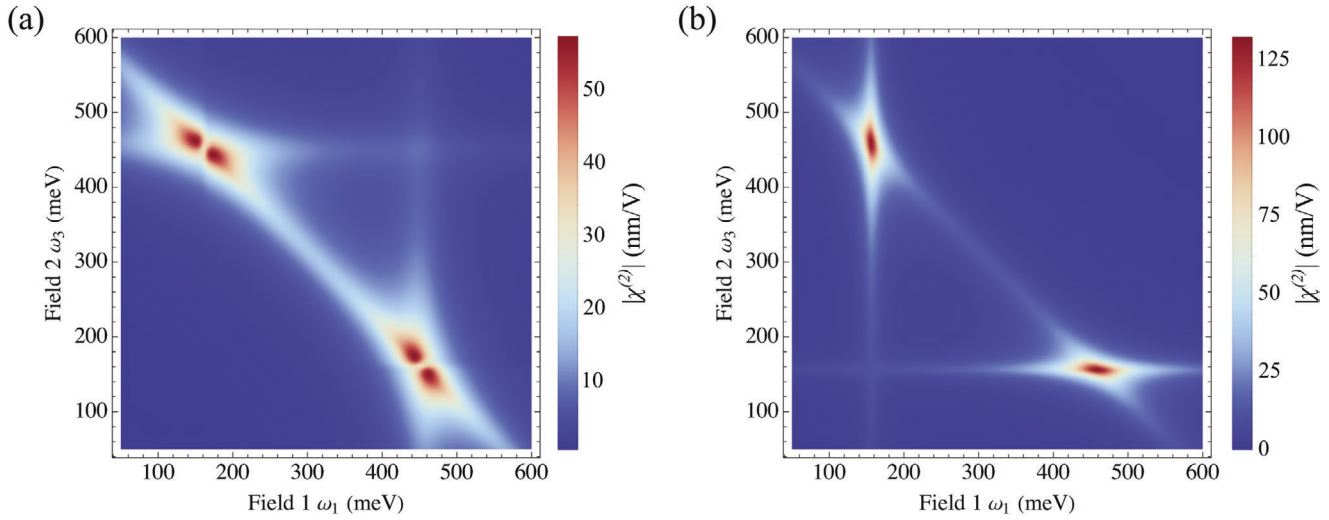

Figure 3. a,b) Nonlinear susceptibility as a function of frequency of incident EM fields calculated for: a) the conventional scheme of pumping the lower transition $1 \rightarrow 2$ (E_1 scheme) (Figure 2a), and b) the proposed scheme of pumping the upper transition $2 \rightarrow 3$ (E_3 scheme) (Figure 2b). The intensity of the strong pumping field is 0.5 MW cm^{-2}

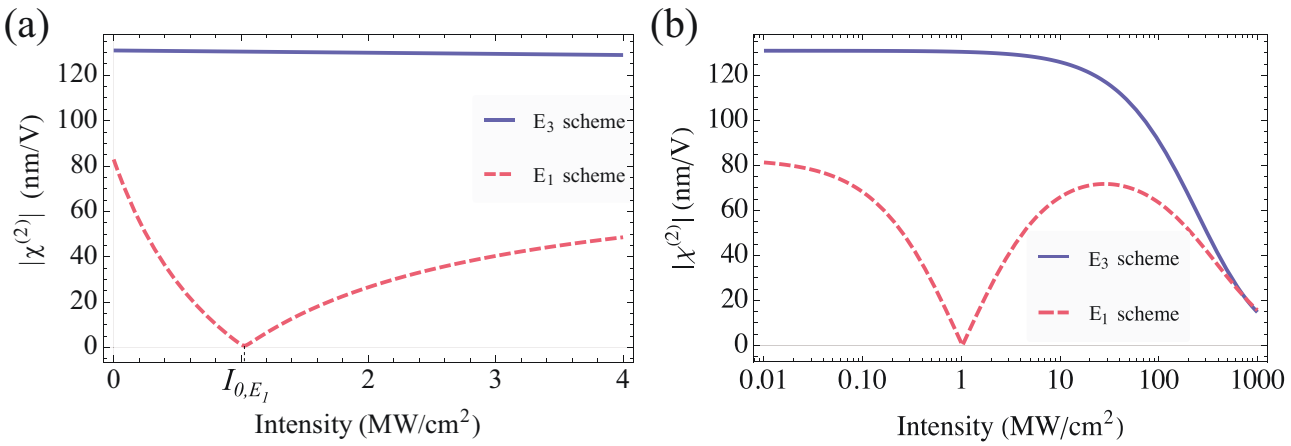

Figure 4. a,b) Second-order nonlinear susceptibilities of the MQW for the E_1 (red dashed line) and E_3 (blue solid line) pumping schemes: a) near the pumping intensity of the $1 \rightarrow 2$ transition saturation; b) at large pumping intensities showing the saturation due to power broadening. The parameters used in the calculations are shown in Table 1.

within the practical pumping regime and is below the damage threshold for the sample.

On the contrary, there are no drastic changes in the dependence of $\chi^{(2)}_{zzz,E_3}$ on I_3 when pumping the upper transition. Only a slight decay is found with increasing pumping intensity (Figure 4a). The absolute value of the second-order nonlinear optical susceptibility remains high, $\approx 125\ \mathrm{nmV^{-1}}$, which is orders of magnitude larger than the second-order nonlinear optical susceptibility of traditional materials.[16] Moreover, the absolute value of $\chi^{(2)}_{zzz,E_3}$ exceeds the values of the nonlinear optical susceptibility in the E_1 pumping scheme over the entire considered range of pumping intensities. Such a drastic difference in nonlinear response of the two nonlinear MQW structures is due to the fact that the strong pump physically transfers electron population from the ground to the first excited state in the E_1 scheme (cf. Figure 2), while in the E_3 scheme, the strong pump mostly leads to intensity broadening of the transition between the electron states 2 and 3, which already has significant broadening due to high electron dephasing rate ($\gamma_{31} \gg r_{21}$, cf. Equations (9) and (10)).

By strong pumping the intersubband transition between the two electron states with negligible electron population, namely, the $2 \rightarrow 3$ transition, we avoid strong intensity saturation (see Equation (10)). The saturation of the $2 \rightarrow 3$ transition occurs only due to the Rabi splitting and happens at much higher pumping intensities (see Figure 4b). Note that this type of saturation occurs in both pumping schemes. The critical value of the pumping field is

$$\mathcal{E}_{0,E_3} = \sqrt{\frac{\hbar^2 \gamma_{31} \gamma_{21}}{4 d_3^2}} \tag{12}$$

obtained from Equation (10). The corresponding local saturation intensity in the semiconductor heterostructure is $I_{0,E_3} \approx 100\ \mathrm{MW\ cm^{-2}}$, which is much larger than the saturation intensity of the $1 \rightarrow 2$ transition in the E_1 pumping scheme, and is typically above the damage threshold of MQW-based metasurfaces, unless very short pulses are used. Thus, for practical levels of continuous-wave pump intensities, we may assume that the E_3 scheme is not affected by intensity saturation.

4. Metasurface Design and Comparison of the two Pumping Schemes

Ultimately, the MQW designs analyzed above are to be integrated into metasurfaces to enable nonlinear optical systems for upconversion that are free from phase matching constraints. In this section, using the $\chi^{(2)}_{zzz}$ expressions (9) and (10) derived in the previous section, we explore optimal metasurface designs for the simultaneous enhancement of the z-components of the electric field in the unit cells at the pump frequency (ω_1 or ω_3), signal frequency (ω_3 or ω_1), and SF at $\omega_2 = \omega_1 + \omega_3$ for the E_1 and E_3 schemes, respectively. Similar, although differently shaped, doubly- and triply-resonant metal nanoresonators filled with MQW semiconductor heterostructures have already been experimentally demonstrated for second harmonic generation and difference-frequency generation in the mid-infrared spectral range.[11,12,27]

We explore an optimized subwavelength modified triod shaped antenna[28] with inversion symmetry in the x-direction and broken inversion symmetry in the y-direction, as shown in **Figure 5**. The x-polarized pump and signal incident waves excite the electric dipole resonances of the triod shape antenna. These resonant excitations lead to z-polarized electric field oscillations in the MQW semiconductor material, which, in turn, generate nonlinear polarization currents oscillating at SF. The nonlinear polarization excites a y-polarized antenna resonant mode tailored to efficiently radiate at SF. The nonlinear process fully takes place locally within the proposed metasurface unit cell, which is deeply subwavelength, therefore freeing the structure of phase-matching constraints. The overall conversion efficiency is only limited by material losses and nonlinear optical susceptibility saturation.

The metasurface unit cell is composed of a metallic ground plane, followed by an MQW layer, and finally a thin gold layer of 100 nm, as shown in Figure 5. The anisotropic optical properties of the MQW are encoded in its dielectric permittivity given by the expression,

$$\varepsilon_{\mathrm{MQW}} = 3.2^2 (\hat{x}\hat{x} + \hat{y}\hat{y}) + \varepsilon_{zz}(I_z(\mathbf{r}))\hat{z}\hat{z} \tag{13}$$

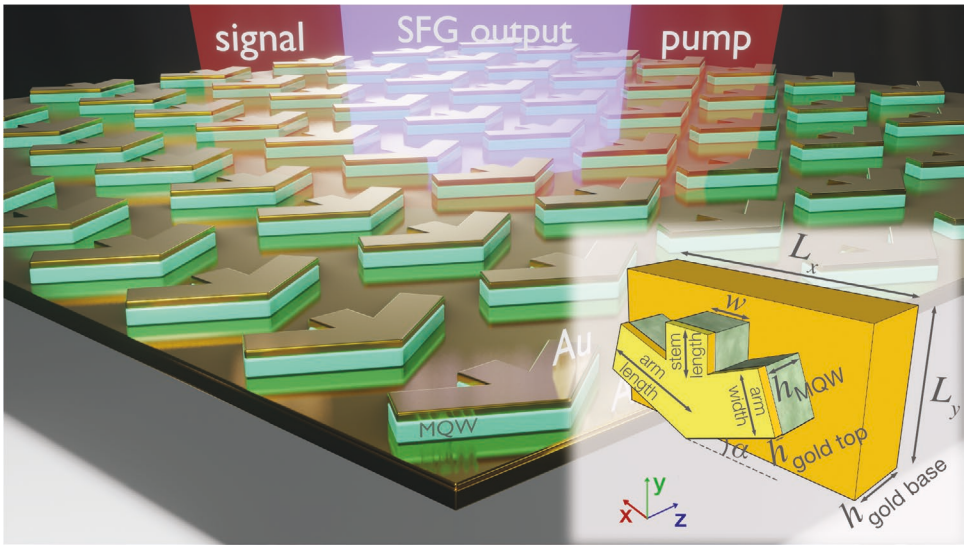

Figure 5. A 3D sketch of the proposed metasurface design and a view of an individual unit cell with labels for dimensions. Both pumping schemes were simulated using nearly the same metasurface dimensions. Specifically, the nanoresonator for the E_1 scheme metasurface used the arm length = 0.8 µm, arm width = 0.268 µm, w = 0.268 µm, h_{MQW} = 0.19 µm, L_x = 1.65 µm, L_y = 0.93 µm, ground plane gold thickness $h_{gold\text{-}base}$ = 0.1 µm, and top gold thickness $h_{gold\text{-}top}$ = 0.1 µm. The nanoresonator dimensions for E_3 scheme is +1.5% of the E_1 scheme dimensions, and the optimal value of α was found to be slightly different for the E_1 and E_3 pumping scheme designs, specifically 21.8 and 31.8°, respectively. The stem lengths are 120 nm for E_1 scheme metasurface, while it is 60 nm for the E_3 scheme.

where $I_z(\mathbf{r}) = 2n_{MQW} \mid E_z^{pump} \mid^2 / Z_0$ is the z-component of the local intensity at position vector $\mathbf{r}$ inside the MQW, n_{MQW} = 3.2 is the refractive index of the MQW for x- and y-polarized electric field, which we assume to be wavelength-independent for simplicity, and $Z_0 = \sqrt{\mu_0 / \varepsilon_0}$. The z-component of the dielectric tensor is considered to be both wavelength- and local-light-intensity-dependent. It is written as,[11,16,28]

$$\varepsilon_{zz}(I_z(\mathbf{r})) = n_{MQW}^2 + \sum \frac{N q_e^2 z_{jk}^2 \mid \rho_{kk}(I_z(\mathbf{r})) - \rho_{jj}(I_z(\mathbf{r})) \mid}{\varepsilon_0 \hbar(\omega_{jk} - \omega - i\gamma_{jk})} \tag{14}$$

where ρ_{jj} are diagonal components of the density matrix and the summation is carried out over the specified indices, $\{j,k\} = (\{2,1\}, \{3,2\}, \{3,1\})$. The optimal parameter values for the metasurface designs tailored for both pumping schemes are given in Table 1. Details of the calculations of the state populations, $N \times \rho_{jj}$, as a function of the local field intensity can be found in the Supporting Information.

In **Figure 6**a,b, we plot the z-component of the dielectric constant of the MQW for the E_1 and E_3 schemes, respectively, and for different homogeneous pump frequency intensity levels in the MQW material. Similar to the strong intensity dependence of the nonlinear susceptibility for the E_1 scheme shown in Figure 4, we observe a strong dependence of the real and imaginary parts of the dielectric constant for the E_1 scheme on the pump wave intensity. Specifically, at the photon energy of the signal wave 156 meV, the absorption increases rapidly with increasing pump intensity for the E_1 MQW design. In contrast, for the E_3 scheme, the change in permittivity for increasing pump intensity is negligible, as shown in Figure 6b. In addition, the losses at the pump frequency in the E_3 scheme are almost negligible, suggesting that we can design very high-Q resonances and exploit a large field enhancement.

To confirm and quantify the enhancement of the z-components of the optical fields by the metasurface at the SFG input and output frequencies, we performed linear full-wave electromagnetic simulations of the E_1 scheme and E_3 scheme metasurface unit cells with periodic boundary conditions in the x and y directions. We assumed a normally incident plane wave with x or y polarization from the port; in the linear simulation, we ignored any intensity dependent changes by either assuming very low incident power of the plane wave, or explicitly turning off the nonlinear sources in the MQW, which is the method we adopted in this simulation. **Figure 7**a,b shows the calculated linear reflection coefficient for the E_1 scheme metasurface for the wavelength ranges relevant to the experimental configuration, specifically the 1.8–3 µm wavelength range in (a) and the 6–9 µm wavelength range in (b). We note that, for the E_1 scheme, the optimal pump wavelength is at λ_{pump} = 2.74 µm, the optimal signal wavelength is at λ_{signal} = 7.66 µm, and the SFG wavelength is at λ_{SFG} = 2 µm. The dips in the simulated power reflection coefficient in Figure 7a,b coincide with the the pump, signal, and SF wavelengths, and a large field enhancement of the z-component of the electric field is observed at all three frequencies of the SFG process, as shown in Figure 7c. The resonance at the long wavelength corresponds to a first-order dipole resonance in the x-direction, while at shorter wavelengths, the resonances correspond to a higher-order dipole resonance. On the contrary, for y-polarization, the resonance at 2 µm is mainly characterized by a first-order dipole resonance along the y-direction. The Rabi splitting around 2.7 µm for x-polarization in Figure 7a indicates strong coupling between the optical dipole mode and the material resonance.

Similarly, Figure 7d,e shows the simulated power reflection coefficients for x- and y-polarized light for the E_3-scheme metasurface. The same wavelength ranges are used for the

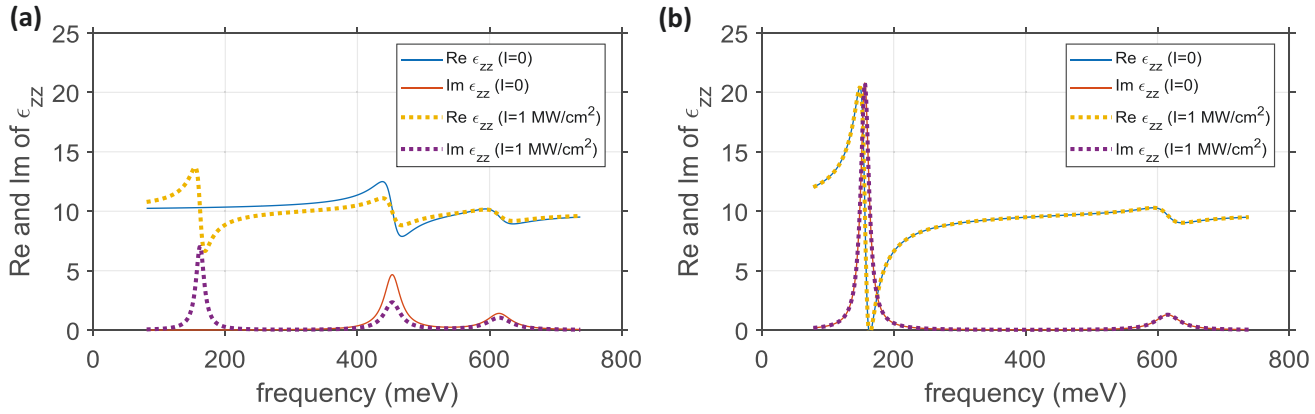

Figure 6. a,b) Vertical (*z*) component of the MQW dielectric constant function versus frequency for different pump intensity levels for the E_1 scheme (a) and the E_3 scheme (b), noting that the curves overlap in case of E_3 scheme.

simulations as in Figure 7a,b. We note that the the optimal pump wavelength λ_{pump} = 2.7 µm, the optimal signal wavelength λ_{signal} = 8 µm, and the SFG wavelength λ_{SFG} = 2 µm for the E_3 scheme are nearly the same as that for the E_1 scheme.

For the case of the E_3-scheme metasurface, the Rabi splitting arises at around 8 µm due to the strong material resonance, as shown in the permittivity function in Figure 6 compared to the Rabi splitting around 2.7 µm for the E_1-scheme metasurface.

In Figure 7f, we plot the field enhancement for the *z*-component of the electric field in the MQW structures at three SFG process wavelengths. Strong field enhancement up to a factor of ≈10 at the pump wavelength is observed, significantly larger than that in the E_1-scheme metasurface. This large pump field enhancement is due to the negligible losses at the pump wavelength in the E_3 scheme MQW. In addition to a dramatic reduction of the nonlinear optical susceptibility saturation (cf. Figure 4), high field enhancement due to low optical losses at the pump frequency represents another remarkable advantage of the E_3 scheme for designing metasurfaces for upconversion. As a result, a relatively small external pumping intensity is needed to achieve strong optical pump fields in the MQW structures for this metasurface design.

To perform nonlinear optical simulations of the upconversion efficiency, we did three coupled frequency domain

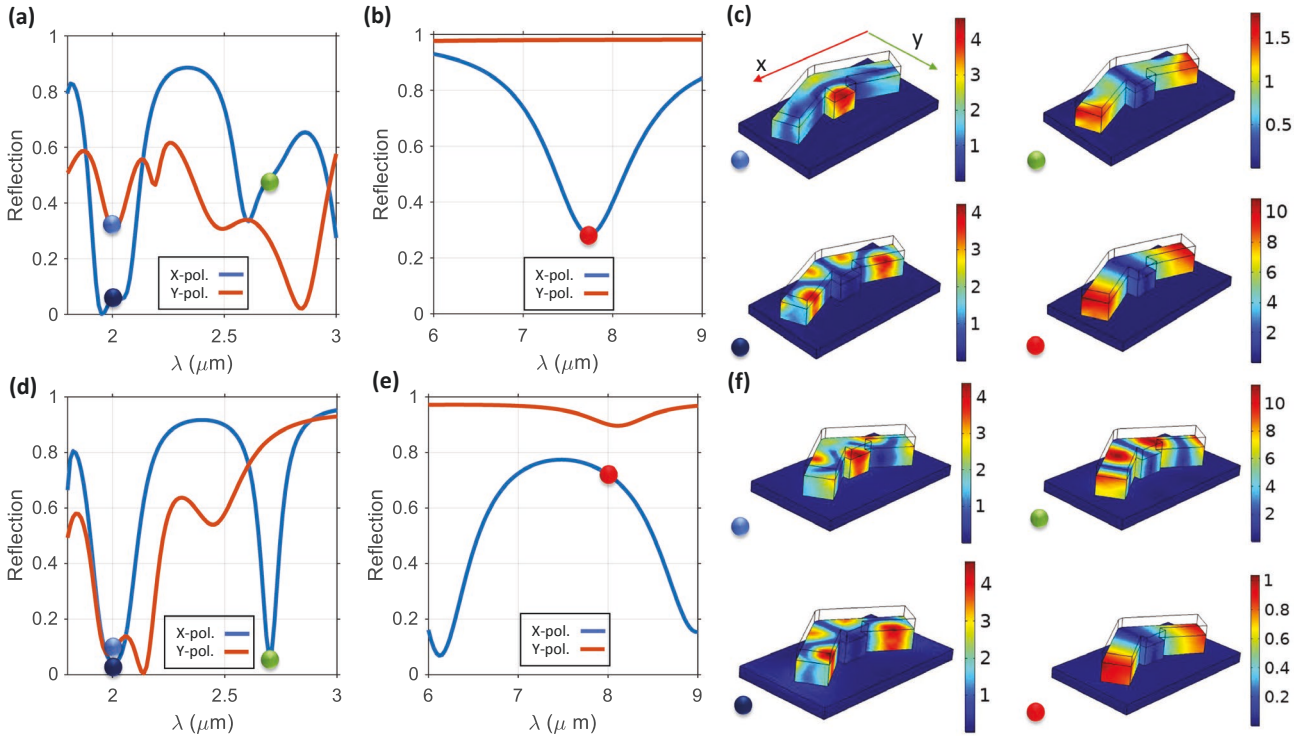

Figure 7. a,b) Calculated linear reflection spectra of the metasurface for the E_1 scheme with different input polarizations. c) Calculated electric field enhancement E_z/E_{inc} for the corresponding points in (a,b). The data points are located at the wavelengths of the pump λ_{pump} = 2.74 µm, the signal λ_{signal} = 7.66 µm, and the SF λ_{SFG} = 2 µm. d–f) Calculations similar to that shown in (a–c) but for the E_3-scheme metasurface. The frequency points for computing the field distribution are located at the wavelengths of the pump λ_{pump} = 2.7 µm, the signal λ_{signal} = 8 µm, and the SF λ_{SFG} = 2 µm.

simulations at the three mixing frequencies, that are the pump frequency, the signal frequency, and the SFG frequency. We first did linear simulation at the signal frequency with *x*-polarized normally-incident plane waves. The signal intensity is fixed at 10^{-4} W cm^{-2} to be consistent with a typical intensity of thermal radiation in thermal imaging systems, and the pump intensity is varied. In parallel, we did a nonlinear simulation at the pump frequency assuming x-polarized normally incident plane wave with high power. The nonlinearity takes place inside the MQW as local change in the dielectric constants of the MQW permittivity tensors, which are significantly varying for E1 scheme under high power. Additionally, for each value of the pump intensity, along with the available results from the first frequency domain simulation, we calculate the nonlinear polarization term inside the MQW as given by Equation (2) in periodic boundary conditions. In the third step, we did frequency domain simulation at the SFG frequency where the nonlinear polarization inside the MQW serves as a source of radiation at the SF wavelength.

We then integrate the radiated power over the surface of one unit cell far from the structure and normalize this power to the unit cell area.[28] Finally, we calculate the SFG upconversion efficiency defined as the intensity of the SFG output divided by the signal beam intensity (Equation (5)).

The results for the upconversion efficiency of both schemes as a function of pump intensity are shown in **Figure 8**. In the simulation, we calculated $\chi^{(2)}$ locally inside the MQW for a given local field intensity at the pump frequency based on Equation (9) for the E_1 scheme and Equation (10) for the E_3 scheme. The local field intensity is enhanced in comparison with the incident pump intensity in $|\mathcal{E}_{loc}/E^{inc}_{pump}|^2$ times. The results show that the maximum upconversion efficiency of ≈4% is achieved for the E_3 scheme for the pump intensity of approximately 1 MW cm^{-2}. In contrast, the E_1 scheme efficiency at the pump intensity below 1 MW cm^{-2} is more than an order of magnitude lower and even vanishes around the pumping intensity of 0.03 MW cm^{-2}, as shown in the inset, due to saturation of the lower, 1 → 2, transition. Note that due to the field enhancement inside the resonators, the pumping intensity required for the 1 → 2 transition saturation is significantly lower than that shown in Figure 4 for a slab of MQW. As we increase the pump power, the efficiency of the E_1 scheme begins to rise again due to the change in sign of the corresponded nonlinear susceptibility (Equation (9)), while the efficiency of the E_3 scheme begins to decline due to the power broadening, Equation (10). Due to the uneven field enhancement within the metasurface and its dependence on the pump intensity, the two efficiency curves intersect at 4.3 MW cm^{-2}. We emphasize that in real experiments such high pump power values are impractical,[11,12] particularly for continuous-wave operation, making the E_3 scheme more promising for use with high efficiency in low power applications.

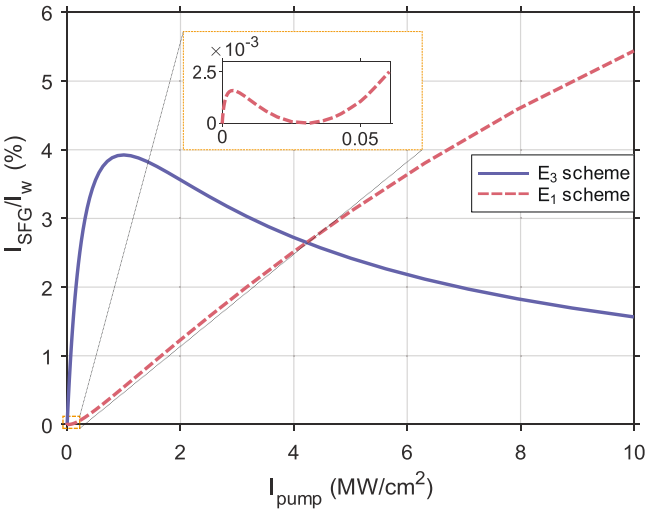

Figure 8. Efficiency of the SFG for E_3 and E_1 schemes versus the pump power while keeping the signal power fixed with $I_w = 10^{-4}$ W cm^{-2}. The inset shows the zoom of the dash box near the origin where it indicates zero efficiency around 0.03 MW cm^{-2}.

The observed difference in the efficiency between the E_1 and E_3 schemes is attributed to two main reasons: the nonlinear susceptibility $\chi^{(2)}$ for the E_1 scheme quickly drops due to intensity saturation of the 1 → 2 intersubband transition (see Figure 4) and the field enhancement of the pumping field in MQW material in the E_1 scheme metasurface is much smaller than that of the E_3 scheme metasurface due to strong absorption at the pump frequency in the former (see Figure 7). Although one can increase the nonlinear optical susceptibility $\chi^{(2)}$ of the E_1 scheme MQW by increasing doping, we cannot avoid the quick reduction of the optical nonlinearity due to intensity saturation and the problem of low pump field enhancement of the E_1 scheme compared to the E_3 scheme.

5. Enhanced SFG Model Including Coulomb Interactions

For a more detailed description of the system including energy renormalization and collective effects, we introduce a model taking into account many-body Coulomb interactions. In the Hartree–Fock approximation, a set of equations similar to the semiconductor Bloch equations (SBEs)[29] can be obtained, except that we are working with intersubband transitions, and the charge density of doping ions needs to be considered. Like in the SBEs, there are two effects from the Coulomb interaction, one is the energy renormalization of the electronic states, and the other is the coupling between the electronic polarizations. The latter effect is generally important when the doping density is extremely high and several subbands are populated.[30] In this work, only the lowest subband is populated, so we expect the main effect of the Coulomb interaction to be the energy renormalization, and the coupling between polarizations can be neglected. Beyond the Hartree–Fock approximation, we include the screening effect coming from higher order correlations.

The details of the calculations are in the Supporting Information. Using this formalism, we calculate the energy renormalization and $\chi^{(2)}$ for realistic structures, with the Coulomb interactions taken into account. As an example, in **Figure 9**, we show the energy renormalization of the structure designed for the E_3 pumping scheme, shown in Figure 1b. The effective masses of the three subbands are found in the band-structure calculation as $\{0.0643, 0.0734, 0.0937\}\times m_0$, where m_0 is the free

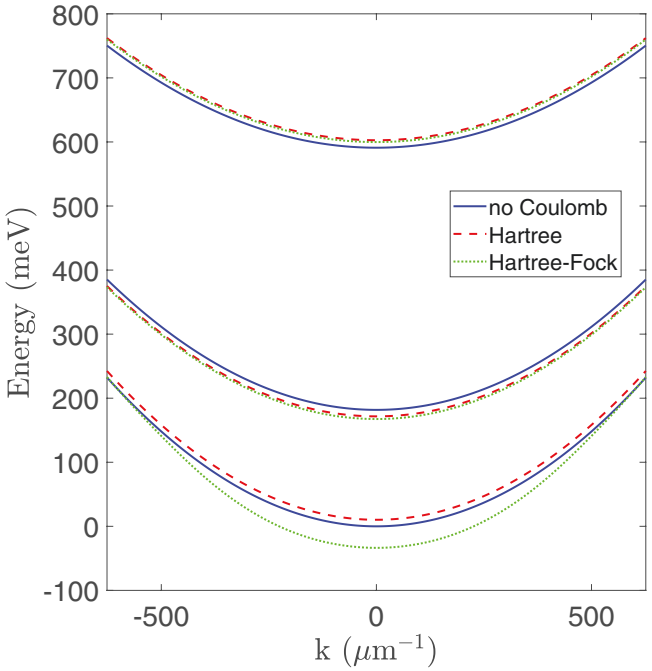

Figure 9. The effect of the Coulomb interactions on the energy renormalization for the heterostructure designed for the E_3 pumping scheme, shown in Figure 1b.

electron mass. For calculation of the Coulomb interaction, the dielectric constant of $\varepsilon = 11.6$ is used for the GaInAs/AlInAs QW, the electronic temperature is 300 K, and the broadenings in the density matrix equations and the expression of polarizability are set to be 10 meV. The Hartree contribution to the energy renormalization is a constant shift for all the *k*-states in a subband. The exchange interaction has a large effect on the lowest subband, where the shift is toward the lower energies and it is *k*-dependent, so the energy dispersion is altered.

To study the effect of the Coulomb interactions on the second-order nonlinear processes, we calculate $\chi^{(2)}$ for the two cases: without and with the Coulomb effects. The result is shown in **Figure 10**. Here, the dephasing rate corresponds to an energy of 10 meV and is assumed to be the same for all the optical transitions. The broadening of the peak of $|\chi^{(2)}|$ is much larger than 10 meV, which is the result of the inhomogeneous broadening caused by the nonparabolicity. With the Coulomb interaction included, the position of the peak is shifted, the broadening is increased, and the magnitude of the peak decreases by about 30%. In this calculation, electrons are assumed to be staying in the lowest subband. For high enough pump powers, electrons can be pumped up to higher subbands even when the pump is off resonance. This will affect the energy renormalization and make the subband positions and dispersion change as a function of the pump power. As a result, one may need to introduce slight tuning of the pump frequency to maintain a given detuning from the corresponding transition. Due to the absence of the $1 \rightarrow 2$ transition saturation, the variation is expected to be weaker when the pump is applied to the empty transition $2 \rightarrow 3$ as in Figure 1b. This is yet another reason in favor of the E_3 scheme. The figures plotted for the E_1 scheme are in the Supporting Information.

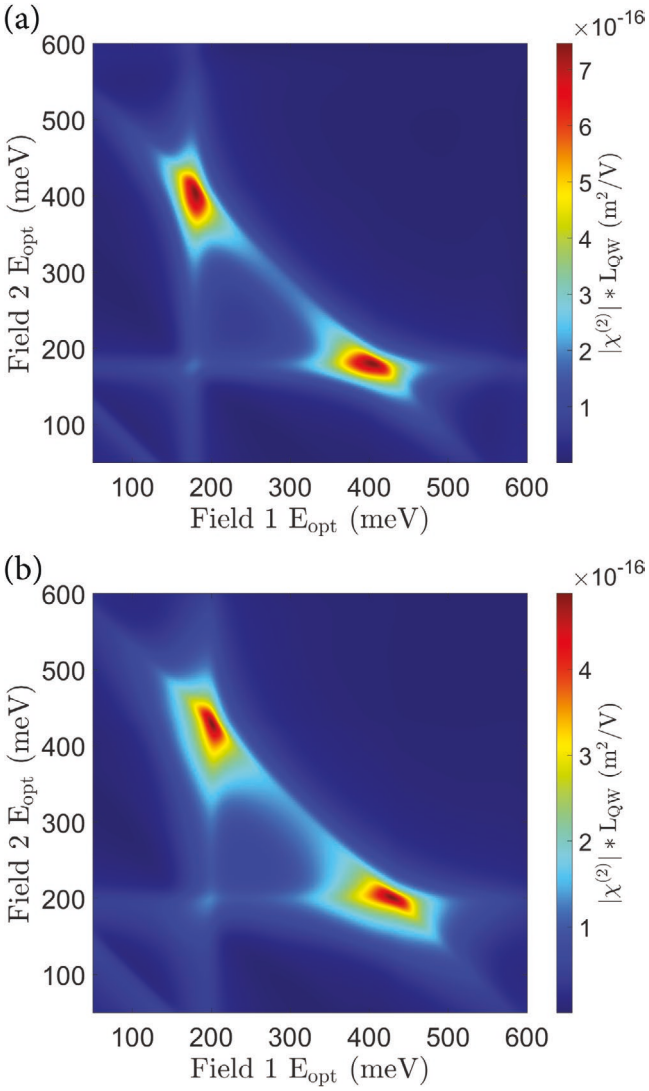

Figure 10. a,b) The second-order nonlinear optical susceptibility calculated without (a) and with (b) Coulomb interactions, for the E_3 scheme structure shown in Figure 1b. The temperature is at 300 K and the Fermi level is at 103 meV above the band edge of the lowest subband.

6. Conclusions

We have introduced and explored an ad hoc pumping scheme for nonlinear MQW metasurfaces that allows extending the intensity levels over which strong nonlinear interactions may be achieved, yielding significantly enhanced efficiency of frequency mixing compared to conventional schemes. We focused on the technologically relevant problem of upconversion of weak mid-infrared signals based on doubly-resonant MQW nonlinearities. Our results show that a strong optical pump field resonant with the intersubband transition between the upper electron states that lack electron population largely enhances the overall achievable efficiency. We performed detailed simulations to confirm that this approach has significant advantages compared to more conventional approaches based on strong resonant pumping of the optical transition

between the ground and excited states. Considerations of the optimal designs involving both material and photonic engineering of the MQW metasurfaces show that, at the pumping intensity of 1 MW cm^{-2} or below, the proposed scheme can provide more than ≈10 times higher upconversion efficiency compared to more conventional nonlinear metasurfaces pumped in resonance with the lower transition. We also confirmed that the effects of many-body Coulomb interactions are not significant in terms of SFG efficiency and the shift in resonances due to these effects can be easily compensated in experiments by a proper choice of pumping frequency.

Overall, our work introduces a concrete strategy to enhance the efficiency of nonlinear metasurfaces, relaxing the severe constraints stemming from material saturation responses. This technique may be extended to other nonlinear processes with, for instance, $\chi^{(3)}$ nonlinearity, and holds the promise to enhance a variety of nonlinear operations enabled by ultrathin metasurfaces, including night-vision imaging, frequency conversion, and wave mixing.

Supporting Information

Supporting Information is available from the Wiley Online Library or from the author.

Acknowledgements

DARPA Nascent, ONR, AFOSR. The work of Y.W. and A.B. was supported in part by NSF Awards No. 2135083 and 1936276.

Conflict of Interest

The authors declare no conflict of interest.

Data Availability Statement

The data that support the findings of this study are available from the corresponding author upon reasonable request.

Keywords

multiple quantum well metasurfaces, nonlinear optical devices, sum-frequency generation

Received: August 31, 2021
Revised: October 29, 2021
Published online:

[1] N. Yu, F. Capasso, *Nature Materials* **2014**, *13*, 139.
[2] J. A. Schuller, E. S. Barnard, W. Cai, Y. C. Jun, J. S. White, M. L. Brongersma, *Nat. Mater.* **2010**, *9*, 193.
[3] L. Novotny, N. Van Hulst, *Nat. Photonics* **2011**, *5*, 83.
[4] G. Li, S. Chen, N. Pholchai, B. Reineke, P. W. H. Wong, E. Y. B. Pun, K. W. Cheah, T. Zentgraf, S. Zhang, *Nat. Mater.* **2015**, *14*, 607.
[5] L. Kang, S. Lan, Y. Cui, S. P. Rodrigues, Y. Liu, D. H. Werner, W. Cai, *Adv. Mater.* **2015**, *27*, 4377.
[6] L. Kang, S. P. Rodrigues, M. Taghinejad, S. Lan, K.-T. Lee, Y. Liu, D. H. Werner, A. Urbas, W. Cai, *Nano Lett.* **2017**, *17*, 7102.
[7] K. Koshelev, S. Kruk, E. Melik-Gaykazyan, J.-H. Choi, A. Bogdanov, H.-G. Park, Y. Kivshar, *Science* **2020**, *367*, 288.
[8] S. A. Maier, *Opt. Express* **2006**, *14*, 1957.
[9] F. Ding, A. Pors, S. I. Bozhevolnyi, *Rep. Prog. Phys.* **2017**, *81*, 026401.
[10] A. Krasnok, M. Tymchenko, A. Alù, *Mater. Today* **2018**, *21*, 8.
[11] J. Lee, M. Tymchenko, C. Argyropoulos, P.-Y. Chen, F. Lu, F. Demmerle, G. Boehm, M.-C. Amann, A. Alù, M. A. Belkin, *Nature* **2014**, *511*, 65.
[12] J. Lee, N. Nookala, J. S. Gomez-Diaz, M. Tymchenko, F. Demmerle, G. Boehm, M.-C. Amann, A. Alù, M. A. Belkin, *Adv. Opt. Mater.* **2016**, *4*, 664.
[13] *Intersubband Transitions in Quantum Wells: Physics and Devices*, (Eds: S. S. Li, Y.-K. Su), Springer, Boston, MA, USA **1998**.
[14] M. Tymchenko, J. S. Gomez-Diaz, J. Lee, M. A. Belkin, A. Alù, *J. Opt.* **2017**, *19*, 104001.
[15] J. S. Gomez-Diaz, M. Tymchenko, J. Lee, M. A. Belkin, A. Alù, *Phys. Rev. B* **2015**, *92*, 125429.
[16] R. W. Boyd, *Nonlinear Optics*, Academic Press, San Diego, CA, USA **2020**.
[17] H. Haug, S. W. Koch, *Quantum Theory of the Optical and Electronic Properties of Semiconductors*, World Scientific Publishing Company, Singapore **2009**.
[18] G. Bastard, *Wave Mechanics Applied to Semiconductor Hetereostructures*, Les Editions de Physique, Paris, France **1992**.
[19] I. Vurgaftman, J. R. Meyer, L. R. Ram-Mohan, *J. Appl. Phys.* **2001**, *89*, 5815.
[20] K. L. Vodopyanov, V. Chazapis, C. C. Phillips, B. Sung, J. S. H. Jr, *Semicond. Sci. Technol.* **1997**, 8.
[21] I. Vurgaftman, J. Meyer, L. Ram-Mohan, *IEEE J. Quantum Electron.* **1996**, *32*, 1334.
[22] A. Belyanin, C. Bentley, F. Capasso, O. Kocharovskaya, M. O. Scully, *Phys. Rev. A* **2001**, *64*, 013814.
[23] H. Fröhlich, *Proc. R. Soc. London, Ser. A* **1952**, *215*, 291.
[24] L. Mandel, E. Wolf, *Optical Coherence and Quantum Optics*, Cambridge University Press, Cambridge. UK **1995**.
[25] M. Kira, S. W. Koch, *Semiconductor Quantum Optics*, Cambridge University Press, Cambridge, UK **2011**.
[26] M. O. Scully, M. S. Zubairy, *Quantum Optics*, American Association of Physics Teachers, College Park, MD, USA **1999**.
[27] Y. Liu, J. Lee, S. March, N. Nookala, D. Palaferri, J. F. Klem, S. R. Bank, I. Brener, M. A. Belkin, *Adv. Opt. Mater.* **2018**, *6*, 1800681.
[28] A. Mekawy, A. Alù, *Nanophotonics* **2021**, *10*, 667.
[29] F. Vasko, A. Kuznetsov, *Electronic States and Optical Transitions in Semiconductor Heterostructures*, Graduate Texts in Contemporary Physics, Springer, New York **2012**.
[30] A. Delteil, A. Vasanelli, Y. Todorov, C. Feuillet Palma, M. Renaudat St-Jean, G. Beaudoin, I. Sagnes, C. Sirtori, *Phys. Rev. Lett.* **2012**, *109*, 246808.